Metabolism 181 (2026) 156648

Contents lists available at ScienceDirect

Metabolism

journal homepage: www.journals.elsevier.com/metabolism

Macrophage-derived SPP1 promotes subretinal fibrosis by YAP1 phase separation in retinal pigment epithelium

Ruoyi Lin [a,b,1], Zixin Cai [c,1], Tianyu Zheng [a,1], Yan Wu [a,b], Zihang Xu [a,b], Yunhong Luo [a,b], Feng Liang [a,b], Manhui Zhu [d,*], Jing Yu [b,e,**], Wenting Cai [a,***]

[a] Department of Ophthalmology, Shanghai Tenth People's Hospital, School of Medicine, Tongji University, Shanghai, China
[b] Department of Ophthalmology, Shanghai Pudong Hospital, Fudan University Pudong Medical Center, Shanghai, China
[c] School of Medicine, Tongji University, Shanghai, China
[d] Department of Ophthalmology, Lixiang Eye Hospital of Soochow University, Suzhou, China
[e] Department of Ophthalmology, the Third People's Hospital of Bengbu, Bengbu, China

ARTICLE INFO

Keywords:
Subretinal fibrosis
Retinal pigment epithelium
Macrophage
Secreted phosphoprotein 1
Yes-associated protein 1

ABSTRACT

Background: Subretinal fibrosis (SRF) is a critical end-stage feature of neovascular age-related macular degeneration (nAMD) with limited treatment options. However, the pathological mechanism during the transformation of choroidal neovascularization (CNV) into SRF remains unclear.
Methods: Bulk RNA-seq of mouse macrophages treated with succinate or lactate in acidic hypoxia identified *Spp1* as a key fibrosis-associated gene. Dynamic Spp1 expression was tracked by single-cell RNA-seq in a CNV model, while laser-induced CNV and SRF models assessed the pro-fibrotic role of Spp1 in vivo. In vitro, the binding of SPP1 to RPE CD44 was identified through bioinformatics and Co-IP, and Western blotting examined downstream CD44/RhoA/YAP1 pathway proteins. qPCR quantified nine YAP1 isoforms to identify the predominant one after SPP1 intervention. The specific YAP1 isoform undergoing liquid-liquid phase separation (LLPS) was determined by visualizing intracellular localization and biomolecular condensates via EGFP-tagged plasmid transfection, with LLPS characteristics confirmed by live-cell imaging and fluorescence recovery after photobleaching (FRAP). ATAC-seq identified the transcription factors co-activated with YAP1 driving fibrosis, while EMT phenotypes were evaluated using pro-fibrotic gene expression, migration, and collagen contraction assays.
Results: Succinate and lactate upregulated Spp1 and activated correlated Ca^{2+} influx pathways. An expanding $Spp1^{+}$ Mφ population was found in early-to-mid CNV. SRF mice showed elevated Spp1in Mφs, and intravitreal Spp1 worsened CNV fibrosis, which blocked by small interfering extracellular matrix receptor III (siCD44). In vitro, SPP1 bound to CD44 activated the RhoA/YAP1 pathway, characterized by a predominant isoform shift from YAP1–1α to YAP1–2α. The nuclear translocation and LLPS of YAP1–2α facilitated pro-fibrotic gene transcription by binding to TEAD4, thereby promoting EMT-like changes in RPE.
Conclusions: Under accumulation of acidic metabolites, SPP1-overexpressing Mφs promote EMT in the RPE via CD44/RhoA-mediated YAP1–2α LLPS. This process involves binding to TEAD4 to co-activate pro-fibrotic gene transcription, revealing novel pathomechanisms involved in SRF progression.

1. Introduction

Neovascular age-related macular degeneration (nAMD) is a leading cause of severe vision loss [1], characterized by choroidal neovascularization (CNV) and often progressing to subretinal fibrosis (SRF) - a major cause of anti-VEGF treatment failure [2]. SRF involves

* Correspondence to: M. Zhu, Lixiang Eye Hospital of Soochow University, Suzhou, 215002, China.
** Correspondence to: J. Yu, Department of Ophthalmology, Shanghai Pudong Hospital, Fudan University Pudong Medical Center, 2800 Gongwei Road, Pudong, Shanghai, 201399, China.
*** Correspondence to: W. Cai, Department of Ophthalmology, Shanghai Tenth People's Hospital Affiliated with Tongji University, 301 Middle Yanchang Road, Shanghai, 200072, China.
E-mail addresses: zhumanhui@suda.edu.cn (M. Zhu), dryujing@aliyun.com (J. Yu), caiwentingtj@163.com (W. Cai).
[1] These authors contributed equally to this work.

https://doi.org/10.1016/j.metabol.2026.156648
Received 9 November 2025; Accepted 15 May 2026
Available online 19 May 2026

extracellular matrix remodeling driven by interactions among macrophages, retinal pigment epithelium (RPE), and myofibroblasts [3]. RPE cells can undergo epithelial-mesenchymal transition (EMT), contributing to fibrosis, while macrophages recruited to hypoxic, acidic CNV microenvironments influence disease progression [4]. In our study, metabolites such as succinate and lactate accumulated in these regions and modulated macrophage-RPE crosstalk.

Macrophages, the most abundant immune cells in fibrotic microenvironments, are heavily recruited to CNV lesions and contribute to pathological angiogenesis, macular hardening, and fibroblast scaffold development [5]. The accumulated macular hardening may reduce the oxygen supply from the choriocapillaris [6]. Under hypoxic and inflammatory conditions, acidic metabolites accumulate, inducing macrophage polarization. CNV membranes with M2 infiltration show greater fibrotic propensity than those with M1 infiltration [7]. Our previous work revealed that the TCA cycle metabolite succinate induced M2 polarization, exacerbating posterior hemorrhage by promoting vascular sprouting [8]. Another key acidic metabolite, lactate, which is known for its roles in cancer immunotherapy, neuroexcitation, and angiogenesis [9,10], was reported to be transported by the RPE from the subretinal space to the choroid [11]. Its accumulation in CNV areas altered macrophage metabolism and promoted endothelial cell angiogenesis [12], increasing the risk of hemorrhage and fibrosis. Thus, investigating macrophage-RPE crosstalk, particularly macrophage-mediated mechanisms in acidic SRF microenvironments, is crucial.

Yes-associated protein 1 (YAP1), a transcriptional coactivator and key Hippo pathway effector, regulates diverse cellular processes, including growth, proliferation and apoptosis. In fibrosis, YAP1 activation is closely associated with myofibroblast proliferation, collagen production, and excessive ECM deposition, all of which are characteristic features of fibrotic tissue [13]. Under stress, YAP1 undergoes nuclear translocation and forms active transcriptional hubs through liquid–liquid phase separation (LLPS), recruiting TEAD4 to modulate target gene transcription [14]. While most studies have focused on the role of total YAP1 expression in stem cell differentiation and oncogene transcription [15–17], the isoform shift of YAP1 and LLPS mechanism in fibrosis remain unclear.

Our research identified $SPP1^{+}$ macrophages as key players in SRF via integrated transcriptomic and single-cell sequencing. Mechanistically, SPP1 upregulated YAP1 expression in the RPE via the CD44/RhoA signaling pathway, and YAP1 promoted RPE-EMT through LLPS-mediated biomolecular condensate formation, with a predominant isoform shift from YAP1–1α to YAP1–2α. The YAP1–2α-TEAD4 complex facilitated pro-fibrotic gene transcription promoting EMT-like changes in RPE and driving SRF progression. This study provides the first demonstration that macrophage-derived SPP1 under acidic hypoxic conditions plays a role in promoting SRF while also revealing the functional significance of YAP1 LLPS in RPE-EMT. These findings offer new insights into the pathogenesis of SRF and reveal potential new therapeutic targets.

2. Materials and methods

2.1. Animals

Male C57BL/6J mice (2 months old) were procured from Shanghai Sipur-Bikai Experimental Animal Co., Ltd. (Shanghai, China). All experimental protocols involving animals were performed in strict compliance with the Association for Research in Vision and Ophthalmology (ARVO) Statement for the Use of Animals in Ophthalmic and Vision Research, with approval granted by the Institutional Animal Care and Use Committee of the Shanghai Tenth People's Hospital affiliated with Tongji University. The animals were maintained under controlled environmental conditions with a 12-h light/dark cycle and provided ad libitum access to standard food and purified water.

2.2. Laser-induced mouse CNV and SRF model

To establish the CNV and SRF models, the animals were systemically anesthetized with 0.5% pentobarbital sodium (Sigma Aldrich, St. Louis, MO, USA) following pupillary dilation via topical tropicamide phenylephrine eye drops (Santen Pharmaceutical Co., Ltd., Osaka, Japan). Laser photocoagulation was performed using a 647 nm laser with a spot size of 50 μm, power of 120 mW, and duration of 100 ms, positioned at the 3, 6, 9, and 12 o'clock positions approximately 2–3 optic disc diameters from the optic nerve head. Immediate bubble formation confirmed successful Bruch's membrane rupture. To establish the SRF model, a secondary laser was applied to each lesion site after a 7-day interval [18]. The experimental groups included the following: (1) normal control; (2) CNV group: sacrificed on day 10 post-laser; (3) CNV + SPP1 group: receiving intravitreal injection of 1 mg/mL SPP1 (1 μL; #94826ES25, Yeasen, Shanghai, China) for 3 consecutive days post-laser and sacrificed on day 10; (4) CNV + SPP1 + siCD44 group: receiving intravitreal injection of 164 nM siCD44 (1 μL) 3 days prior to laser followed by the SPP1 intravitreal injection as above and sacrificed on day 10; and (5) SRF group. Four mice were used per group in each experiment.

2.3. Fundus fluorescein angiography (FFA) assessment

Following CNV and SRF induction, comprehensive retinal vascular evaluation was conducted through FFA. After general anesthesia and complete pupillary dilation were achieved, the mice received intraperitoneal administration of fluorescein sodium (5 μg/g; #46960, Sigma Aldrich, St. Louis, MO, USA). Retinal imaging was performed via a Phoenix Micron IV retinal imaging microscope at 5-min post-injection. The quantitative assessment of fluorescein leakage was conducted via ImageJ software.

2.4. Immunofluorescence staining of choroidal flat mounts

Following cervical dislocation to obtain mouse eyeballs, enucleated eyes were processed for choroidal flat-mount preparation. This involved anterior segment removal followed by a four-leaf pattern relaxation incision in the sclerochoroidal-RPE complex. Immunofluorescence staining was performed by incubating the tissues for 24 h at 4 °C with Alexa Fluor 488-labeled isolectin B4 (1:200; #I21411, Thermo Fisher Scientific, Massachusetts, USA) for vascular labeling and α-smooth muscle actin (α-SMA) primary antibody (1:500; #GB111364-100, Servicebio, Wuhan, China) followed by a Cy3-conjugated goat anti-rabbit secondary antibody (#111-165-003, Jackson ImmunoResearch, West Grove, PA, USA) for fibrosis visualization.

2.5. Hematoxylin–eosin (H&E) staining

For H&E staining, ocular specimens were collected and immediately fixed in 4% paraformaldehyde (PFA). Tissue processing involved dehydration with graded ethanol (70%, 80%, 95%, and absolute alcohol; 1–2 h per concentration) followed by xylene clearing (two changes, 15 min each). Paraffin infiltration was performed via standard embedding cassettes, with subsequent sectioning at 2 μm thickness along the optic axis. Deparaffinized sections were stained with hematoxylin (5 min), rinsed until the optimal purple hue developed (50 s), differentiated in 1% acid–alcohol (3 s), and blued in running water (50 s). Counterstaining was performed with eosin (1 min) and distilled water rinses, followed by ethanol dehydration, xylene clearing, and neutral resin mounting. Histological evaluation was conducted via a Leica DM6 B microscope (Leica Microsystems, Wetzlar, Germany).

2.6. Masson's trichrome staining

Masson's trichrome staining was performed following the

manufacturer's protocol (#G1345, Solarbio Science & Technology Co., Ltd., Beijing, China). The tissue sections were fixed with Bouin's fluid prior to sequential staining with (1) celestine blue and Mayer's solutions for the nucleus, (2) phosphomolybdic acid and aniline blue for the collagen fibers, and (3) ponceau-fuchsin solutions for the other components. The processed slides were dehydrated and mounted for brightfield microscopy.

2.7. Cell culture

ARPE-19 and THP-1 cell lines (Zhongqiao Xinzhou Biotechnology, Shanghai, China) were maintained in DMEM/F12 and RPMI-1640 media, respectively, supplemented with 10% fetal bovine serum (FBS, Gibco, Carlsbad, CA, USA) and penicillin–streptomycin (100 U/mL-100 μg/mL). THP-1 differentiation into macrophages was achieved through exposure to 100 ng/mL phorbol 12-myristate 13-acetate (PMA; ECS001, Shanghai Yishan Biotechnology Co., Ltd., Shanghai, China) for 48 h.

2.8. Isolation of primary mouse peritoneal macrophages

Peritoneal macrophages were isolated from C57BL/6J mice following a standardized protocol [19]. The animals received daily intraperitoneal injections of 6% starch broth (1 mL per administration) for three consecutive days to elicit macrophage recruitment. Forty-eight hours after the final injection, peritoneal lavage was performed via ice-cold RPMI-1640 medium, with multiple washes to ensure complete cell retrieval. The collected lavage fluid was centrifuged at 300 $\times g$ for 5 min, after which the supernatant was carefully aspirated and discarded. The resulting cell pellet was resuspended in serum-free RPMI-1640 basal medium and subsequently plated in 6-well culture plates. Following a 6-h incubation period at 37 °C with 5% CO_2 to allow for macrophage adherence, nonadherent cells were removed by gently washing the plates 2–3 times with serum-free RPMI-1640 medium. This purification process yielded an enriched population of peritoneal macrophages, which were then maintained in complete RPMI-1640 medium supplemented with 10% FBS for subsequent experimental procedures. We subsequently treated isolated primary mouse peritoneal macrophages with either 1 mM succinate for 48 h or 20 mM lactate for 6 h in separate experimental groups.

2.9. Bioinformatic analysis

For this study, scRNA-seq data from the GEO database entry “GSE222094” were utilized. The data were comprehensively preprocessed via the Seurat R package (version 4.3.0). First, potential doublets were removed with DoubletFinder, and certain genes were filtered out. The data were then normalized and reduced via principal component analysis (PCA). To correct for batch effects, the “Harmony” package was employed. The “FindVariableFeatures” function was used to refine the dataset and identify genes with high variability. After cell sorting, advanced dimensionality reduction techniques such as UMAP were applied for further analysis. Marker genes were identified by consulting cell marker databases and relevant literature. Finally, the pseudotemporal trajectories of cell development were visualized via Monocle2.

Total RNA was extracted from primary cells, succinate-treated cells, and lactate-treated cells for genome-wide transcriptomic analysis. The RNA sequencing libraries were constructed via the SureSelect XT HS2 mRNA Library Preparation Kit (Agilent, Santa Clara, CA, USA), with up to 1 μg of total RNA input, following the manufacturer's instructions. The bulk RNA-sequencing data generated by the Illumina NovaSeq 6000 platform were analyzed via Partek Flow software (version 10.0.22.0121; Partek, Inc., St. Louis, MO, USA). Base calling was performed with Illumina Real-Time Analysis software (RTA3, v3.4.4), and FASTQ files were generated via bcl2fastq (version 2.20.0.422). Prior to alignment, the FASTQ files were trimmed at both ends to remove reads with Phred quality scores below 35. Sequence reads were mapped to the human genome GRCh38 via STAR 2.7.8a with default settings. After alignment, the final BAM files were quantified via the Partek E/M algorithm and annotated with Ensembl Transcripts release 102 to generate gene counts. These counts were normalized, and differential gene expression analysis was conducted with DESeq2 to compare lactate-treated, succinate-treated, and primary mouse peritoneal macrophages. Genes with log2-fold changes greater than 1 or less than −1 and a P value less than 0.05 were considered differentially expressed. The differentially expressed genes (DEGs) were then subjected to gene ontology (GO) pathway analysis, Kyoto Encyclopedia of Genes and Genomes (KEGG) analysis, and heatmap generation.

2.10. SiRNA transfection

siRNAs targeting CD44 were designed and synthesized by Sangon Biotech (Shanghai, China). The specific siRNA sequences used in this study were as follows: siNC (forward 5′-UUCUCCGAACGUGUCACGUTT-3′ and reverse 5′-ACGUGACACGUUCGGAGAATT-3′), siCD44#1 (forward 5′-GGUUGUUUCUACCAUCAGA-3′ and reverse 5′-UCUGAUGGUAGAAACAACC-3′), siCD44#2 (forward 5′-CCAUCUGUGCAGCAAACAA-3′ and reverse 5′-UUGUUUGCUGCACAGAUGG-3′), and siCD44#3 (forward 5′-CAGAAAGGAGAAUACAGAA-3′ and reverse 5′-UUCUGUAUUCUCCUUUCUG-3′).

2.11. Plasmid transfection

The pEGFP-C1-YAP1 plasmid was provided by IBSBIO Technology Co., Ltd. (Shanghai, China). The complete plasmid sequence was detailed in Fig. S1. Plasmid transfection was performed via Lipofectamine 3000 transfection reagent (#L3000008, Thermo Fisher Scientific, Massachusetts, USA) according to the manufacturer's recommended protocol.

2.12. Phase separation assay in live cells

ARPE-19 cells expressing pEGFP-YAP1 were plated on confocal imaging dishes (801,002, Nest Biotechnology, Wuxi, China) and allowed to adhere under standard culture conditions. Live-cell imaging was initially performed in phosphate-buffered saline (PBS) via a confocal microscope (LSM900, Carl Zeiss, Jena, Germany). The medium was subsequently replaced with PBS containing 5% (w/v) 1,6-hexanediol, and sequential imaging was performed at predetermined time intervals to assess LLPS dynamics.

2.13. Fluorescence recovery after photobleaching (FRAP) analysis

FRAP experiments were conducted via a Carl Zeiss LSM900 confocal microscope (100× oil immersion objective). Defined regions containing YAP1 condensates were photobleached with a 488-nm laser at 100% power. Post-bleach recovery kinetics were documented through time-lapse imaging over 60 s at 1-s intervals. Quantitative analysis of the fluorescence intensity recovery curves was performed via ImageJ software.

2.14. RNA isolation and quantitative PCR (qPCR) analysis

Total RNA was extracted from cultured cells following established protocols. After experimental treatment, the cells were washed three times with RNase-free PBS prior to RNA extraction via an RNA-Quick purification kit (RN001, Shanghai Yishan Biotechnology Co., Ltd., Shanghai, China). The RNA purity and concentration were determined spectrophotometrically (NanoDrop 3300, Thermo Fisher Scientific). cDNA synthesis was performed with 1 μg of total RNA via HiScript III reverse transcriptase (R312–01, Vazyme, Nanjing, China), followed by quantitative PCR amplification with gene-specific primers (Sangon

Biotech, Shanghai, China) and ChamQ Universal SYBR qPCR Master Mix (Q711–03, Vazyme, Nanjing, China) on a QuantStudio Dx platform (Thermo Fisher Scientific, Massachusetts, USA). Relative mRNA expression levels were calculated via the ΔΔCt method. The primer sequences were shown in Table S1.

2.15. Protein extraction and Western blotting (WB)

Cultured cells in 6-well plates were lysed with 80 μL of ice-cold RIPA buffer containing protease inhibitors (100:1 ratio). After a 1-h incubation on ice, the lysates were centrifuged at 12000 rpm for 30 min at 4 °C. Protein concentrations were determined via a BCA assay (P0011, Beyotime, Shanghai, China), with equal amounts (30 μg) of denatured protein separated via electrophoresis. Following transfer to nitrocellulose membranes, overnight incubation at 4 °C was performed with primary antibodies against SPP1 (1:1000; 22952-1-AP, Proteintech), Arg1 (1:4000; 16001-1-AP, Proteintech), FN1 (1:2000; 15613-1-AP, Proteintech), α-SMA (1:5000; 4395-1-AP, Proteintech), CD44 (1:20,000; 15675-1-AP, Proteintech), YAP1 (1:2000; 13584-1-AP, Proteintech), and RhoA (1:1000; AF6352, Affinity), with GAPDH (1:50,000; 60004-1-Ig, Proteintech) used as a loading control. The membranes were incubated with IRDye® 800CW-conjugated secondary antibodies (goat anti-rabbit, 926-32211; goat anti-mouse, 926-32212; LI-COR Biosciences, Nebraska, USA) and visualized via the Odyssey CLx imaging system (LI-COR Biosciences, Nebraska, USA), with quantitative analysis performed via Image Studio Lite software. All experiments included triplicate biological replicates.

2.16. Immunofluorescence staining

The cell samples were permeabilized and blocked with 0.1% Triton X-100 and 3% bovine serum albumin (BSA) in PBS for 1 h before they were incubated with primary antibodies against FN1 (1:100; 15613-1-AP, Proteintech) and α-SMA (1:500; GB111364-100, Servicebio) at 4 °C overnight. For fluorescence detection, species-specific secondary antibodies conjugated to Alexa Fluor® 488 or Cy3 (Jackson ImmunoResearch) were used, and nuclear counterstaining was performed via DAPI (Sigma, St. Louis, Missouri, USA). Mounted samples were imaged via a Leica DM6 B upright fluorescence microscope (Leica, Wetzlar, Germany).

2.17. Wound healing assays

ARPE-19 cells were cultured in 6-well plates to establish confluent monolayers prior to experimental interventions. A standardized wound was created via a sterile 200 μL pipette tip, followed by three washes with PBS to eliminate cellular debris. To isolate the effects of migration on proliferation, the cultures were maintained in serum-free DMEM/F12. Wound closure dynamics were documented at 0-, 24-, and 48-h timepoints via an Eclipse Ti2 inverted microscope (Nikon, Japan). Quantitative analysis involved calculating the relative wound area reduction: $[1 - (\text{Area}_t / \text{Area}_0)] \times 100\%$ through ImageJ, with triplicate measurements per condition.

2.18. Cell migration analysis

For Transwell assays, treated macrophages were suspended in serum-free medium and loaded into 8-μm pore transwell chambers (3422, Corning, New York, USA). The lower compartment contained 600 μL of complete medium as a chemoattractant. Following 48 h of incubation, nonmigratory cells were mechanically removed from the upper membrane surface. Transmigrated cells were fixed with 4% PFA, stained with 0.1% crystal violet (C0121, Beyotime, Shanghai, China), and imaged via the aforementioned microscope system. Migration indices were derived by counting cells in three randomized microscopic fields per membrane via ImageJ.

2.19. Collagen contraction assays

ARPE-19 cells (2×10^5 cells/mL) were embedded in 2 mg/mL rat tail type I collagen matrix (04167170, Corning, New York, USA) neutralized with 0.1 M NaOH and polymerized in 24-well plates (500 μL/well) at 37 °C for 1 h. After gelation, DMEM/F12 medium supplemented with 10% FBS was added, and the collagen gels were gently released from the plate bottom by circumferentially detaching the edges via a sterile 1 mL pipette tip. Contraction kinetics were monitored at 48 h under standard culture conditions. The gel areas were quantified via ImageJ to determine the relative contraction ratios: (Initial area - Final area)/Initial area × 100%.

2.20. ATAC sequencing and analysis

For chromatin accessibility profiling, human ARPE-19 cells were cultured and exposed to 0.1 μg/mL recombinant SPP1 for 48 h; untreated cells served as controls. Approximately 100,000 cells per condition were collected and pelleted by centrifugation. Cell pellets were lysed in ATAC-seq lysis buffer (10 mM Tris-HCl, 10 mM NaCl, 3 mM $MgCl_2$, and 0.5% NP-40). Nuclei were isolated by centrifugation at 1500 $\times g$ for 5 min at 4 °C. The supernatant was removed, and nuclei were mixed with tagmentation reagents TruePrep® DNA Library Prep Kit V2 for Illumina (Vazyme, TD501-01) at 37 °C for 30 min. Fragmented DNA was purified using the MinElute PCR Purification Kit (QIAGEN). Sequencing libraries were constructed via Illumina Novaseq 6000 platform. Raw sequencing reads were processed using fastx (version: 0.0.13) to yield high-quality clean reads. Clean reads were mapped to the GRCh38 human reference genome utilizing Bowtie (version: 0.12.8). The resulting alignments were stored in BAM format. For peak identification, MACS (version: 2.2.7.1) was executed on each individual BAM file. Annotation of the identified peaks was performed using ChIPseeker (version: 1.30.3). Differentially accessible regions were strictly defined as those exhibiting a minimum of a two-fold change versus the control. Finally, de novo motif discovery was conducted using the findMotifsGenome.pl script from the HOMER package.

2.21. Statistical analysis

Statistical analyses were conducted via SPSS version 24.0 (IBM Corporation, Armonk, NY, USA) for data processing, with graphical representations generated through GraphPad Prism 9 (GraphPad Software, San Diego, CA, USA). Intergroup comparisons were evaluated through Student's *t*-test, while multiple groups were compared via one-way analysis of variance (ANOVA). Statistical significance was established at a threshold probability value of $P < 0.05$ for all hypothesis testing.

3. Results

3.1. Macrophages exhibit calcium overload and secrete SPP1 under acidic metabolic condition

We treated primary mouse peritoneal macrophages with either 1 mM succinate for 48 h or 20 mM lactate for 6 h in separate experimental groups. In the succinate-treated group, we identified 1016 DEGs (Fig. 1A), whereas in the lactate-treated group, we identified 4158 DEGs (Fig. 1B), with 594 genes being commonly altered in both groups (Fig. 1C). To investigate the impact of macrophage-derived factors on adjacent cellular components within the comprehensive immune microenvironment, we intersected these DEGs with secretory protein genes from SPRomeDB and fibrosis-related genes from FDRdb, yielding 4 candidate genes (Fig. 1D). Among these genes, *Spp1*, *Edn1*, and *Igf1* were consistently upregulated by both succinate and lactate treatment, with Spp1 exhibiting the most significant upregulation (Fig. 1E), leading us to select it as the key gene for further investigation. KEGG pathway

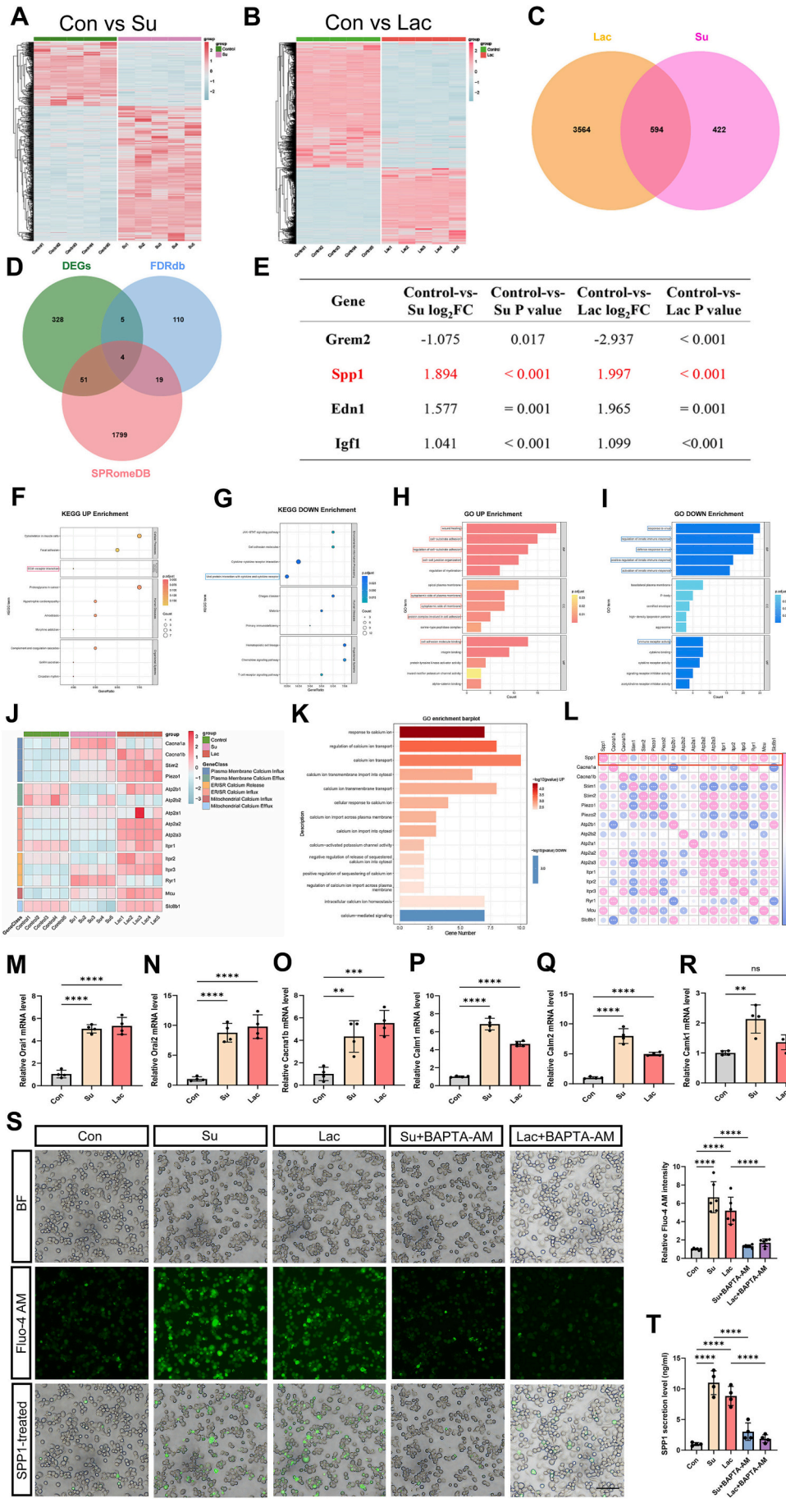

Gene	Control-vs-Su log_2FC	Control-vs-Su P value	Control-vs-Lac log_2FC	Control-vs-Lac P value
Grem2	-1.075	0.017	-2.937	< 0.001
Spp1	1.894	< 0.001	1.997	< 0.001
Edn1	1.577	= 0.001	1.965	= 0.001
Igf1	1.041	< 0.001	1.099	<0.001

(caption on next page)

Fig. 1. Bulk RNA sequencing analysis of primary peritoneal macrophages from mice treated with succinate and lactate. (A) Heatmap displaying differentially expressed genes (DEGs) in the succinate-treated group compared with the control group. (B) Heatmap showing DEGs in the lactate-treated group compared with the control group. (C) Venn diagram illustrating overlapping DEGs between succinate and lactate interventions. (D) Fibrosis-related secretory protein genes identified from the DEG pool. (E) Detailed $\log_2$(fold changes) (log2FC) and *P* values of fibrosis-related secretory protein DEGs following succinate and lactate treatments. (F) Upregulated pathways enriched by KEGG analysis of fibrosis-related secretory protein DEGs. (G) Downregulated pathways enriched by KEGG analysis of fibrosis-related secretory protein DEGs. (H) Upregulated pathways identified through GO enrichment analysis of fibrosis-related secretory protein DEGs. (I) Downregulated pathways revealed by GO enrichment analysis of fibrosis-related secretory protein DEGs. (J) Expression profiles of calcium signaling-related DEGs, including genes involved in plasma membrane calcium ion influx/efflux, ER/SR calcium ion release/influx, and mitochondrial calcium ion influx/efflux. (K) Significantly enriched calcium signaling pathways identified through GO analysis (upregulated pathways marked in red and downregulated pathways marked in blue). (L) Correlation analysis demonstrating co-expression patterns between Spp1 and calcium signaling genes. (M-R) qPCR validation of the gene expression levels of calcium ion influx channel genes (Orai1, Orai2, and Cacna1b), and calcium-regulating genes (Calm1, Calm2, and Camk1). (S) Representative fluorescence images (left) and quantification (right) of intracellular calcium ion levels in macrophages, labeled with Fluo-4 AM. Scale bar: 50 μm ($n = 6$). (T) ELISA quantification of SPP1 secretion in macrophages ($n = 4$). The data in (M-T) were analyzed via one-way ANOVA with Bonferroni analysis. *$P < 0.05$. **$P < 0.01$. ***$P < 0.001$. ****$P < 0.0001$. (For interpretation of the references to color in this figure legend, the reader is referred to the web version of this article.)

analysis revealed the upregulation of ECM-receptor interaction pathways and the downregulation of immune-related pathways (viral protein interactions with cytokines and cytokine receptors) (Fig. 1F–G). GO enrichment analysis revealed the upregulation of pathways associated with cellular migration and tissue repair (such as wound healing, cell–substrate adhesion, plasma membrane cytoplasmic side localization, and cell adhesion molecule binding), along with the downregulation of immune response pathways (response to virus, regulation of the innate immune response, and immune receptor activity) (Fig. 1H–I). These findings collectively indicate that acidic metabolic conditions induce a phenotypic shift in macrophages toward enhanced reparative activity concomitant with immunosuppressive characteristics. Interestingly, we observed that a substantial portion of the DEGs were associated with calcium signaling pathways. Further functional classification revealed the upregulation of genes regulating plasma membrane calcium ion influx, endoplasmic reticulum (ER)/sarcoplasmic reticulum (SR) calcium ion release, and ER/SR calcium ion influx, whereas genes controlling plasma membrane calcium ion efflux were downregulated (Fig. 1J). GO analysis further enriched the upregulation of calcium ion importing into the cytosol, suggesting the occurrence of intracellular calcium overload (Fig. 1K). Correlation analysis revealed significant positive co-expression relationships between *Spp1* and calcium signaling genes, most notably with the mitochondrial calcium uniporter gene *Mcu* (Pearson $r = 0.81$, $P < 0.001$) and the voltage-gated calcium channel subunit gene Cacna1b (Pearson $r = 0.78$, $P < 0.001$) (Fig. 1L). Results of qPCR confirmed significant upregulation of calcium ion influx channel genes (*Orai1*, *Orai2*, and *Cacna1b*), and calcium-regulating genes (*Calm1*, *Calm2*, and *Camk1*) following treatment with acidic metabolites (Fig. 1M–R). These findings suggest that calcium overload in macrophages may be a key mechanism mediating *Spp1* upregulation.

To validate the functional implications of calcium dysregulation, we measured intracellular calcium ion levels using the fluorescent probe Fluo-4 AM. Consistent with our RNA-seq predictions, stimulation with succinate and lactate led to a robust increase in intracellular calcium ion fluorescence intensity, indicating a state of calcium overload in macrophages (Fig. 1S). This was accompanied by a significant elevation in SPP1 protein secretion as measured by ELISA (Fig. 1T). To determine whether calcium overload is a requisite signal for SPP1 induction, we pre-treated macrophages with 10 μm BAPTA-AM for 2 h to chelate calcium ion. The decrease in intracellular calcium ion markedly suppressed the acid-induced secretion of SPP1. Collectively, these results demonstrate that acidic metabolites drive SPP1 expression through a calcium ion-dependent signaling mechanism.

3.2. Single-cell RNA sequencing reveals that Spp1$^+$ macrophages are key cellular players in CNV progression

Through systematic analysis of the GSE222094 dataset ($n = 4$), we employed standardized single-cell analytical pipelines (Seurat v4.0) to identify 12 major cell clusters via UMAP dimensionality reduction and the Louvain clustering algorithm (Fig. 2A). Monocytes, macrophages, and microglia subsequently re-clustered into a mononuclear phagocyte population, which was further subdivided into 12 functionally distinct subpopulations on the basis of highly expressed marker genes. Notably, Cluster 4 (11.16% of the total) was characterized by specific high expression of *Spp1* and *Vegfa* and was thus identified as the Spp1$^+$ pro-CNV macrophage subpopulation (Fig. 2B). In the laser-induced CNV model (wild-type + laser group), the proportion of the Spp1$^+$ subpopulation significantly expanded (Fig. 2C, WT: 5.44% vs CNV: 27.19%, $P < 0.001$). GO enrichment analysis demonstrated that this subpopulation was strongly associated with tissue remodeling, positive regulation of the p38MAPK pathway, and cytokine production (Fig. 2D). Key regulatory factor analysis revealed marked activation of *Fabp5*, *Ccr2*, and *Vegfa* in this subpopulation. Pseudotemporal trajectory analysis via Monocle2 indicated that Spp1$^+$ macrophage infiltration primarily occurred during the early-to-mid stages of CNV progression (pseudotime score = 0.00000–17.46096) (Fig. 2E), with differentiation trajectories closely aligned with State1 and CNV group cell distribution patterns (Fig. 2F–I), suggesting their crucial role in CNV advancement. Parallel analysis of Ccr2$^{-/-}$ mice revealed reduced Spp1$^+$ macrophage infiltration post-laser (Fig. S2A), with differentiation trajectories corresponding to State 2 and primarily distributed during the middle–late CNV stages (Fig. S2B–H). These findings collectively indicate that Spp1$^+$ macrophages are rapidly recruited and activated upon CNV initiation, functioning as a major infiltrating population that mediates tissue repair and fibrotic responses.

3.3. Spp1$^+$ macrophages promotes SRF through the SPP1-CD44 interaction

Protein–protein interaction network analysis via Cytoscape (based on the STRING database) revealed direct binding between SPP1 and CD44 (Fig. 3A). We further validated this interaction through co-immunoprecipitation assays (Fig. 3B). We subsequently investigated the functional role of the SPP1-CD44 interaction throughout disease progression via mouse models of CNV and SRF accumulation. The experimental procedures for inducing CNV and SRF were illustrated in Fig. 3C. The CNV model was established via single-laser burning, with observations commencing 10 days post-injury, and the SRF model was generated via two-phase laser burning with a 7-day interval between procedures, followed by a 10-day observation period. Multiplex immunofluorescence analysis of choroidal and retinal tissues revealed distinct pathological features between the two models. In the CNV model, macrophages infiltrated the subretinal space by breaching the choroidal barrier. Notably, the fibrotic lesions in the SRF model contained abundant Spp1$^+$ macrophages, and their population significantly increased during the progression from CNV to SRF (Fig. 3D). To investigate the role of SPP1 in this pathological process, we administered intravitreal injections of 1 μL of SPP1 (1 mg/mL) for three consecutive days following single laser induction. Multiple examinations on day 10 post-laser revealed SRF-like alterations in the CNV lesions. HE staining

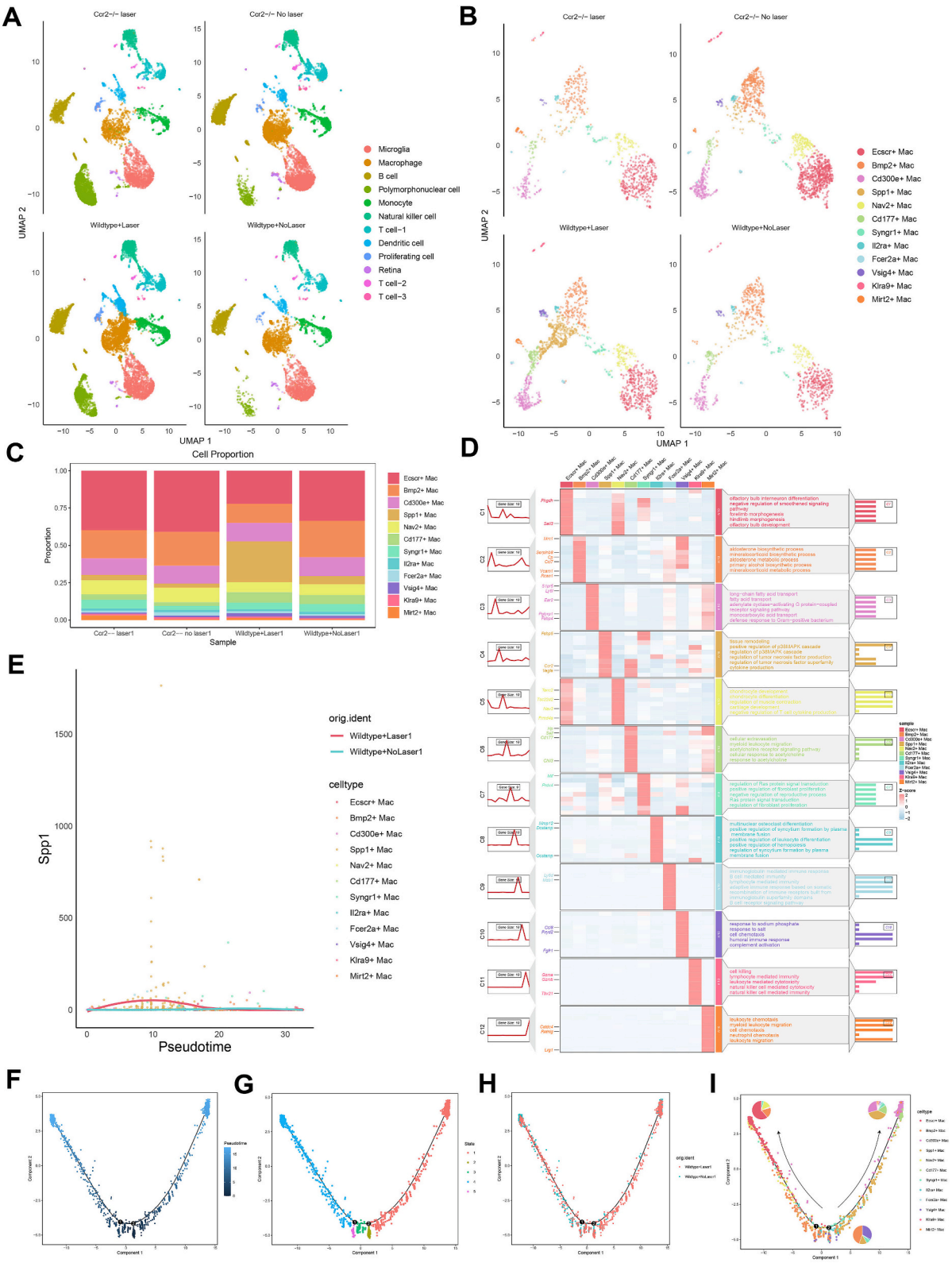

Fig. 2. scRNA-Seq analysis revealing the role of Spp1^{+} macrophage populations in the laser-induced CNV mouse model. (A) UMAP visualization of 12 distinct cell subpopulations. (B) Dimension reduction analysis identifying 12 annotated cell types within mononuclear phagocytes. (C) Stacked bar plot displaying the proportional distribution of mononuclear phagocyte subpopulations (relative to total cell counts per cluster) on the y-axis. (D) Functional characterization of mononuclear phagocyte subpopulations through their top marker genes and pathway enrichment profiles. (E) Pseudotemporal expression patterns of Spp1 in the laser-induced group versus the wild-type group. (F) Pseudotime distribution map along the cellular trajectory. (G) Cell state distribution patterns across the trajectory. (H) Distribution mapping of different treatment groups along the trajectory. (I) Cell type distribution of mononuclear phagocyte subpopulations along the trajectory.

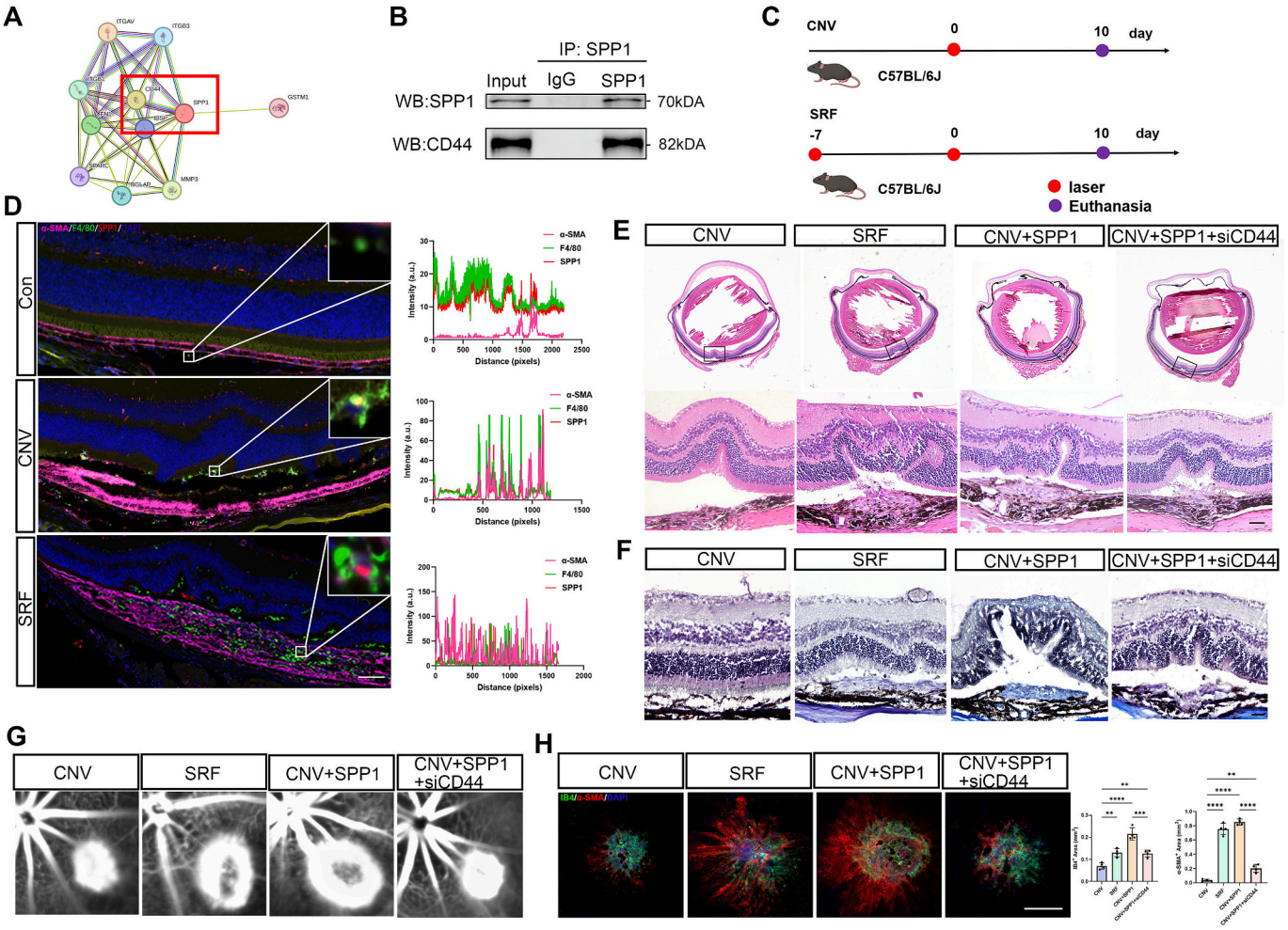

Fig. 3. The impact of SPP1 intervention on the CNV mouse model. (A) Protein-protein interaction network analysis centered on Spp1 and Cd44 via the STRING database. (B) Co-immunoprecipitation assays validating the interaction between SPP1 and CD44. (C) Schematic workflow of CNV and SRF laser-induced modeling. (D) Multicolor immunofluorescence staining showing α-SMA (magenta), F4/80 (green), and SPP1 (red) with DAPI counterstaining (blue), which was used to quantify protein expression in retinal and choroidal tissues. Scale bar: 100 μm (n = 4). (E) Representative hematoxylin–eosin (HE)-stained images of retinal sections from different intervention groups. Scale bar: 20 μm (n = 4). (F) Representative Masson's trichrome staining images of retinal sections from different intervention groups. Scale bar: 20 μm (n = 4). (G) Representative fluorescein fundus angiography (FFA) images across different intervention groups (n = 4). (H) Representative immunofluorescence images of choroidal flat mounts showing CNV lesions and fibrotic foci in the control and treatment groups. Scale bar: 200 μm (*n* = 4). The data in (H) were analyzed via one-way ANOVA with Bonferroni analysis. $^{*}P < 0.05$. $^{**}P < 0.01$. $^{***}P < 0.001$. $^{****}P < 0.0001$. (For interpretation of the references to color in this figure legend, the reader is referred to the web version of this article.)

revealed vascular breakthrough of Bruch's membrane with cellular infiltration at the breach sites (Fig. 3E). Masson's trichrome staining further confirmed the presence of collagen fibers within these breached areas (Fig. 3F). Fluorescein fundus angiography (FFA) revealed enlarged leakage zones surrounding the CNV, with a central hypofluorescent area, suggesting the possible presence of fibrotic tissue that impeded fluorescein perfusion (Fig. 3G). Choroidal flat-mount analysis revealed significant increases in both $IB4^{+}$ and α-SMA-positive areas, indicating enhanced fibrotic responses (Fig. 3H). Importantly, these SRF-like pathological changes were effectively suppressed when the animals were pretreated with CD44 siRNA via intravitreal injection for three days prior to laser induction. These findings strongly suggest that macrophages promote SRF progression through the Spp1-Cd44 signaling axis.

3.4. Succinate and lactate induce M2 polarization and SPP1 overexpression in macrophages, promoting EMT in RPE cells

In vitro experiments demonstrated that treating THP-1-derived human macrophages with 1 mM succinate for 48 h or 20 μM lactate for 6 h significantly increased the protein expression levels of both SPP1 and Arg1 (Fig. 4A). Flow cytometry analysis revealed that treatment with these two acidic metabolites significantly upregulated CD206 expression on THP-1-derived macrophages, whereas CD86 levels remained unchanged (Fig. 4B). This phenotypic shift indicated polarization toward the M2 macrophage subtype, known for its pro-reparative functions, which aligned with our previous findings. Further investigation demonstrated that treatment of ARPE-19 cells with different concentrations of recombinant SPP1 protein for 48 h induced the upregulation of fibrosis markers. Western blot analysis revealed that the most significant increase in the expression of the fibrotic indicators FN-1 and α-SMA occurred at 0.1 μg/mL SPP1 (Fig. 4C), and this concentration was consequently selected for subsequent experiments. Immunofluorescence staining further confirmed substantial fibrosis development in RPE cells at this concentration, as indicated by the increased expression of both FN-1 and α-SMA (Fig. 4D). To assess functional alterations, we conducted wound healing (Fig. 4E), transwell migration (Fig. 4F), and collagen contraction assays (Fig. 4G). The results consistently demonstrated that SPP1 treatment markedly enhanced the cellular migration capacity and collagen contractility, suggesting that SPP1 facilitates EMT

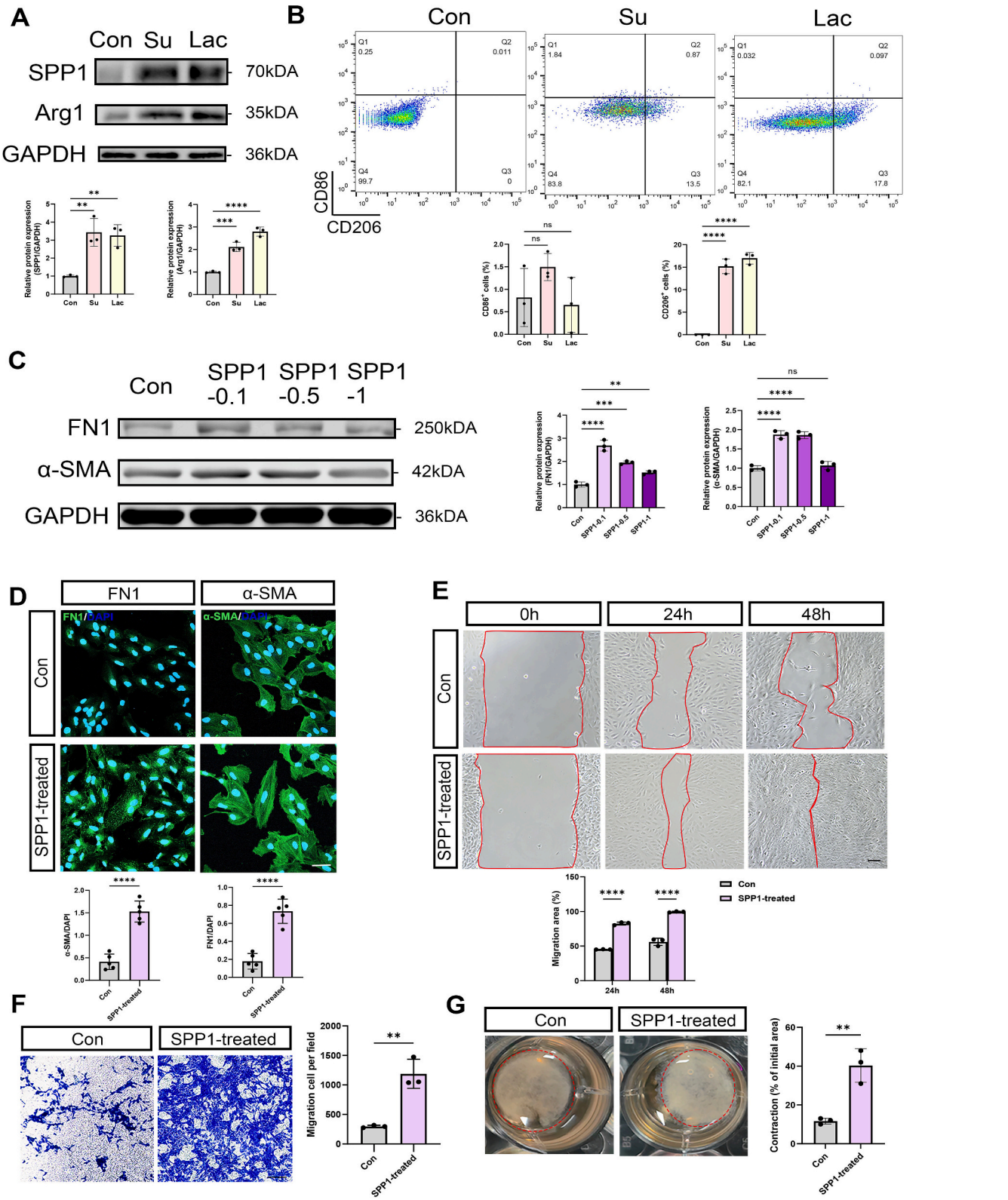

Fig. 4. The impact of macrophage-secreted SPP1 on RPE cells. (A) Western blot analysis of SPP1 and Arg1 expression in THP-1 cells treated with succinate and lactate. (B) Flow cytometry analysis showing significant upregulation of the M2 marker CD206. (C) Western blot analysis of the expression of the fibrosis-related proteins FN1 and α-SMA in ARPE-19 cells treated with different concentrations of SPP1. (D) Immunofluorescence staining of the fibrosis-related proteins FN1 and α-SMA in ARPE-19 cells treated with 0.1 μg/mL SPP1. Scale bar: 20 μm. (E) Representative images of wound healing assays in different ARPE-19 treatment groups, demonstrating cell migration across the wound area at 24 and 48 h post-treatment ($n = 3$). Scale bar: 50 μm. (F) Representative images of Transwell migration assays in different ARPE-19 treatment groups, showing cell migration across the membrane at 48 h post-treatment ($n = 3$). Scale bar: 50 μm. (G) Representative images comparing collagen gel contraction between the control and SPP1-treated groups at 48 h after released from culture plates (n = 3). The data in (A–C) were analyzed via one-way ANOVA with Bonferroni analysis. Other data were analyzed by two-tailed Student *t*-test. $^{*}P < 0.05$, $^{**}P < 0.01$, $^{***}P < 0.001$, $^{****}P < 0.0001$.

progression.

3.5. CD44/RhoA/YAP1 pathway mediates RPE-EMT

CD44 knockdown in RPE cells was achieved via siRNA. qPCR analysis revealed that sequence #3 presented the highest knockdown efficiency (Fig. 5A), which was subsequently used for further experiments. In fibrotic diseases, CD44 functions as a YAP1-regulated transmembrane adhesion receptor that is upregulated in fibroblasts in response to mechanical stress and matrix stiffness through Rho GTPases [20,21]. We therefore hypothesized that SPP1 activates YAP1 via CD44/RhoA signaling to promote RPE-EMT. Western blot analysis confirmed that CD44 knockdown suppressed SPP1-induced upregulation of both RhoA and YAP1 (Fig. 5B), establishing CD44 as the upstream regulator of this pathway. Functional assays demonstrated that CD44 knockdown attenuated SPP1-stimulated RPE migration (Fig. 5C–D) and collagen contraction capacity (Fig. 5E). Immunofluorescence analysis of YAP1 localization revealed that SPP1 treatment triggered significant nuclear translocation of YAP1 and the subsequent formation of biomolecular condensates within the nuclei. Importantly, CD44 knockdown eliminated these effects, and SPP1 supplementation failed to restore them (Fig. 5F). Given that SPP1, in addition to binding CD44, signals through

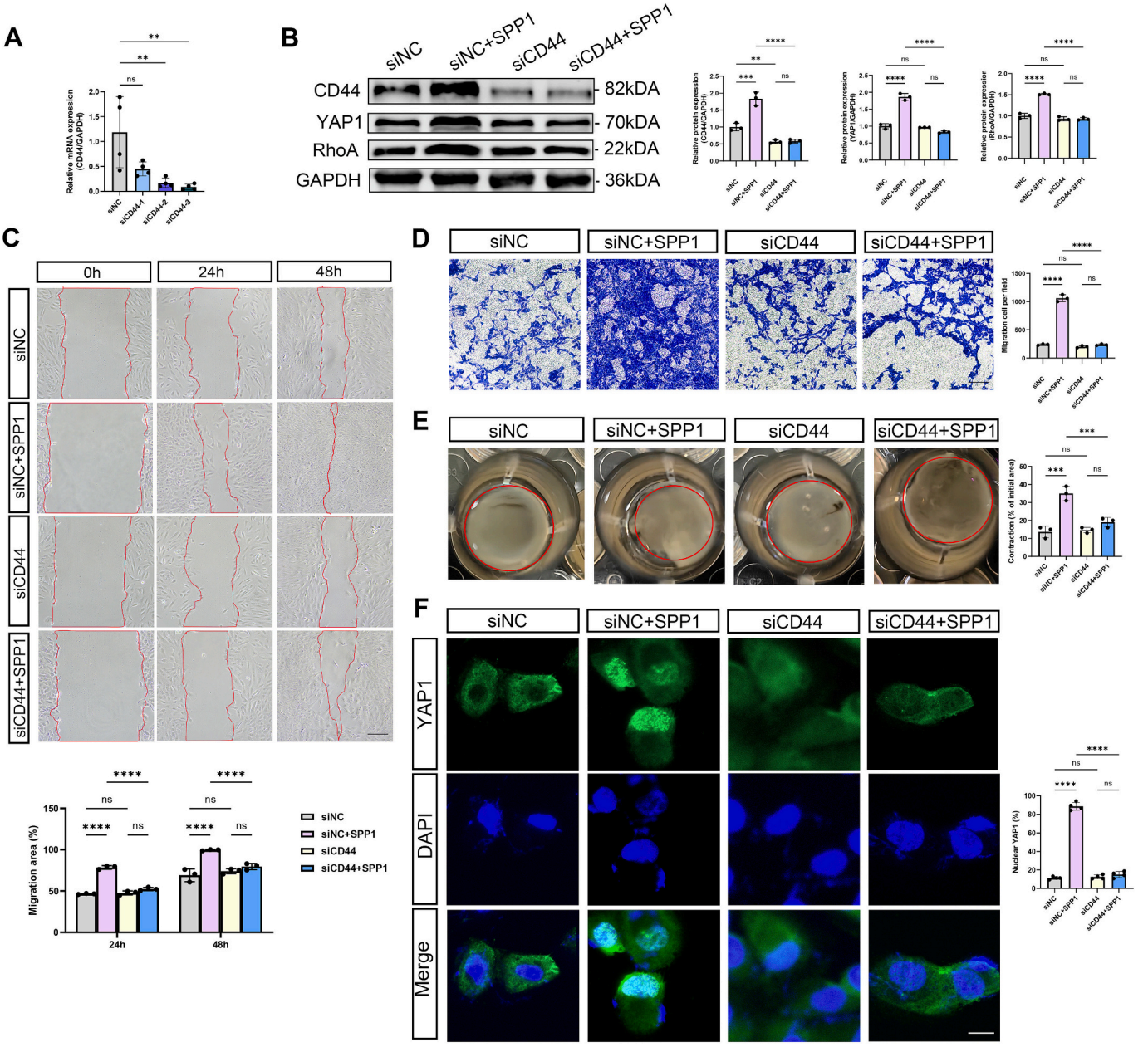

Fig. 5. Molecular mechanisms underlying SPP1-mediated promotion of RPE-EMT. (A) qPCR analysis demonstrating the mRNA expression levels of CD44 following siRNA-mediated knockdown. (B) Western blot analysis of CD44, YAP1, and RhoA protein expression across the four experimental groups. (C) Representative images of wound healing assays in different ARPE-19 treatment groups showing cell migration progression at 24 and 48 h post-treatment (n = 3). Scale bar: 50 μm. (D) Representative images of Transwell migration assays in different ARPE-19 treatment groups, illustrating cellular migration across the membrane at 48 h post-treatment (n = 3). Scale bar: 50 μm. (E) Representative images comparing collagen gel contraction in different ARPE-19 treatment groups at 48 h post-release from culture plates (n = 3). (F) Representative immunofluorescence images showing the subcellular localization of YAP1 (green) in RPE cells. Nuclei were counterstained with DAPI (blue). Scale bar: 10 μm. The data were analyzed via one-way ANOVA with Bonferroni analysis. *$P < 0.05$, **$P < 0.01$, ***$P < 0.001$, ****$P < 0.0001$. (For interpretation of the references to color in this figure legend, the reader is referred to the web version of this article.)

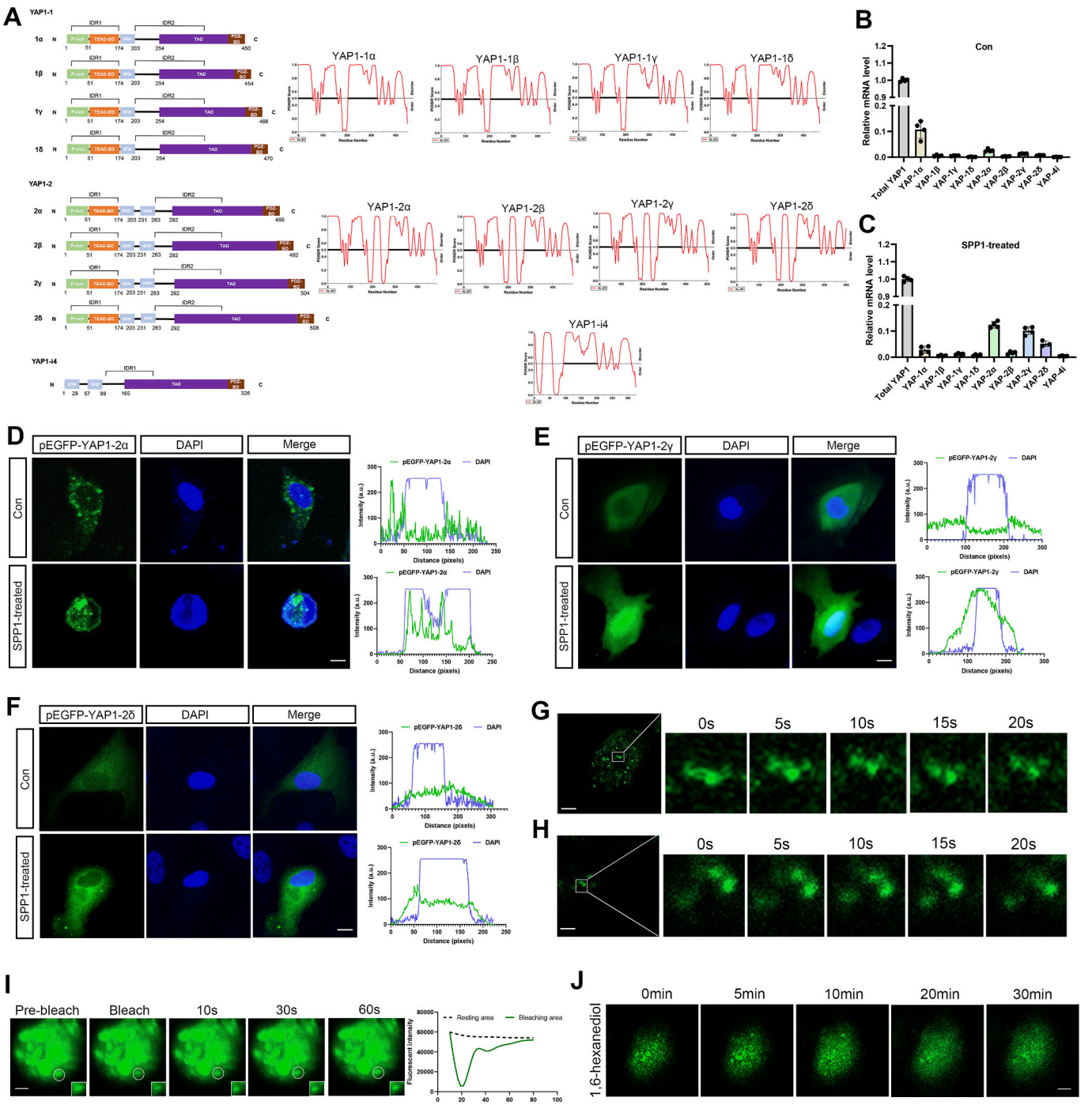

Fig. 6. YAP1 nuclear translocation and condensate formation in RPE-EMT progression. (A) Intrinsically disordered region (IDR) analysis of nine YAP1 isoforms via the Predictor of Natural Disordered Regions (PONDR) database, with regions scoring ≥0.5 considered disordered. (B) mRNA expression levels of the nine human YAP1 isoforms under physiological condition. (C) mRNA expression levels of the nine human YAP1 isoforms under SPP1-stimulated condition. (D) Subcellular localization of YAP1–2α visualized via confocal microscopy following pEGFP-C1 plasmid transfection. Scale bar: 10 μm. (E) Subcellular localization of YAP1–2γ visualized via confocal microscopy following pEGFP-C1 plasmid transfection. Scale bar: 10 μm. (F) Subcellular localization of YAP1–2δ visualized via confocal microscopy following pEGFP-C1 plasmid transfection. Scale bar: 10 μm. (G) Live-cell imaging of pEGFP-YAP1-transfected ARPE-19 cells showing YAP1 droplet fission dynamics via confocal microscopy. Scale bar: 2 μm. (H) Live-cell imaging of pEGFP-YAP1-transfected ARPE-19 cells demonstrating YAP1 droplet fusion events via confocal microscopy. Scale bar: 2 μm. (I) Quantitative fluorescence recovery after photobleaching (FRAP) analysis of YAP1 condensates, with white circles indicating photobleached regions. Scale bar: 2 μm. (J) Representative images comparing the morphology of the YAP1 condensate with 1,6-hexanediol treatment (5%, 0–30 min). Scale bar: 2 μm. $^{*}P < 0.05$, $^{**}P < 0.01$, $^{***}P < 0.001$, $^{****}P < 0.0001$.

multiple integrins via its arginine-glycine-aspartic acid (RGD) motif, we further examined the expression profiles of the integrin family. SPP1 treatment significantly upregulated the expression of integrin subunits ITGAV, ITGB1, and ITGB3 (Fig. S3A). However, inhibition of αv-integrins, β1-integrin, and β3-integrin by using their respective specific inhibitors MK-0429, FNIII14, and myr-RGT failed to suppress the SPP1-induced enhancements in RPE migration and collagen contraction capacity (Fig. S3B–D). Taken together, these results confirm that the

CD44/RhoA/YAP1 axis, rather than integrin signaling, is the primary driver of EMT progression.

3.6. YAP1–2α nuclear translocation and condensate formation promote RPE-EMT

YAP-1 has nine distinct mRNA splicing isoforms [22]. Analysis via the PONDR database revealed two intrinsically disordered regions (IDRs) within the TEAD-binding and transcriptional activation domains of YAP1–1 and YAP1–2 and identified one IDR in YAP1-i4 (Fig. 6A). We quantified the expression levels of the nine human YAP1 isoforms under both physiological and SPP1-stimulated conditions. We found that YAP1–1α is the most abundant isoform in normal RPE cells (Fig. 6B). However, SPP1 treatment significantly altered this profile, upregulating the expressions of YAP1–2α, YAP1–2γ, and YAP1–2δ, with YAP1–2α becoming the predominant isoform (Fig. 6C). Confocal imaging revealed that both YAP1–2α (Fig. 6D) and YAP1–2γ (Fig. 6E) underwent significant nuclear translocation following SPP1 treatment. In contrast, the subcellular localization of YAP1–2δ showed no significant changes after SPP1 treatment (Fig. 6F). Among the isoforms that entered the nucleus, only YAP1–2α formed distinct condensates, whereas YAP1–2γ exhibited a diffuse distribution throughout the nucleus. Live imaging captured fusion/fission events of nuclear YAP1–2α droplets (Fig. 6G–H), whereas fluorescence recovery after photobleaching (FRAP) experiments revealed fluorescence recovery within 60 s postbleaching (Fig. 6I). These condensates were disrupted by 5% 1,6-hexanediol treatment (Fig. 6J), confirming the classic LLPS properties.

3.7. YAP1–2α drives the transcription of pro-fibrotic genes by binding with TEAD4 to their chromatin accessible regions

Given the absence of DNA-binding domains in YAP1, these observed nuclear droplets necessitate association with transcription factors to exert their function [23]. To investigate specific transcription factors, ATAC-seq was performed on RPE cells following a 48-h intervention with the recombinant SPP1 protein. The sequencing data exhibited excellent quality and typical transcription start site (TSS) enrichment profiles. Compared with the control group, the SPP1-treated group displayed higher and more concentrated accessibility signal peaks around the TSS (Figs. 7A, S4A), along with a broader overall distribution pattern (Fig. 7B), indicating a global increase in open chromatin regions across the genome. Additionally, the SPP1 treatment group showed an increased proportion of peaks located in intronic regions, suggesting that changes in chromatin accessibility were primarily concentrated in introns. This may promote the transcriptional activation of genes by increasing the open chromatin state of enhancer regions (Figs. 7C, S4B). We further employed HOMER software to perform motif enrichment analysis on the differentially peaks. The results demonstrated a high enrichment of the binding motif for the transcription factor TEAD4 within the regions that were significantly more open in the SPP1-treated group (Fig. 7D). Cross-referencing with public ChIP-seq databases confirmed the presence of high-confidence TEAD4 binding sites within these differentially accessible regions. Integrative Genomics Viewer (IGV) visualization provided direct evidence that SPP1 exposure markedly enhanced chromatin accessibility of target genes, including *COL4A1*, *COL11A1*, *CXCL8*, *FNBP1*, and *ROCK1* (Figs. 7E, S4C). Immunofluorescence colocalization confirmed that SPP1 promoted the physical interaction between YAP1–2α and TEAD4. Treatment with 10 μM verteporfin (VP), a YAP1–2α-TEAD interaction inhibitor, the SPP1-induced nuclear accumulation of YAP1–2α remained persistent, indicating that VP might not prevent the nuclear translocation of YAP1 but specifically interfered with its binding to TEAD4. Similarly, treatment with 5% 1,6-hexanediol, which specifically disrupts LLPS, led to the diffusion of YAP1–2α within the nucleus and inhibited the interaction between YAP1–2α and TEAD4 (Fig. 7F). Both treatments significantly inhibited the formation of nuclear YAP1-TEAD4 condensates and subsequently attenuated EMT-related phenotypes, including RPE migration (Fig. 7G–H), contractility (Fig. 7I), and the expression of pro-fibrotic genes identified in above ATAC-seq analysis (Fig. 7J–N). These findings suggest that YAP1 LLPS plays a pivotal role in driving RPE-EMT, with YAP1-TEAD4 interaction further promoting its nuclear condensation and pro-fibrotic gene expression.

4. Discussion

In this study, we employed integrated transcriptomic and single-cell RNA sequencing to identify significant enrichment of $SPP1^+$ macrophages within the hypoxic, acidic, proangiogenic microenvironment. These macrophages promoted RPE-EMT through paracrine signaling. SPP1, also known as osteopontin, is a secreted phosphoprotein involved in various biological processes, including cell adhesion, immune regulation, and tissue remodeling. While $SPP1^+$ macrophages are typically categorized as a subclass of tumor-associated macrophages, they have been increasingly identified in non-cancerous conditions such as rheumatoid arthritis, myocardial infarction, and liver cirrhosis [24–26]. Across nearly all existing literature, fibrosis emerged as a defining feature of the $SPP1^+$ macrophages in diverse non-cancerous diseases [27]. Our study reveals for the first time that these cells are also central in the pathological process of SRF, thereby extending the disease spectrum of $SPP1^+$ macrophages to fundus fibrotic conditions.

The increased SPP1 secretion we observed in calcium-dysregulated macrophages was consistent with findings from multiple fibrosis models [28–30]. While previous research has demonstrated that extracellular calcium signals could trigger the differentiation of monocytes into SPP1-producing macrophages [31], we revealed that macrophages were also susceptible to intracellular calcium overload induced by acidic metabolites. This phenomenon had a direct causal relationship with SPP1 secretion, as the use of calcium chelators to inhibit this overload led to a synchronized decline in SPP1 levels. Previous study has established that these two metabolites can activate various calcium channels, such as TRPM2 and Piezo1, thereby triggering calcium ion influx [32,33]. The regulation of SPP1 by calcium ions occurs at both the transcriptional and post-translational levels. Elevated intracellular calcium ion could activate the IKK/NF-κB pathway, directly driving *Spp1* transcription [34,35]. Furthermore, calcium ion influx was closely linked to the dephosphorylation of SPP1 [36]. Beyond calcium signaling, the acidic microenvironment may also synergistically upregulate *SPP1* through pH-sensitive microRNAs, such as miR-203/215 [37]. In summary, succinate- and lactate-mediated SPP1 upregulation in our study was confirmed to be achieved via calcium overload, but other mechanisms remain to be further investigated.

To investigate the role of acidic metabolites in SRF, macrophages were treated with succinate and lactate, both of which accumulate significantly in the CNV microenvironment. There is an inherent difference between the average concentrations of succinate and lactate measured at the tissue level and the concentrations required for functional in vitro interventions. For succinate, the average succinate concentration in the vitreous fluid was reported to be 1.27 μM in patients with epiretinal membranes (ERM) and 2.20 μM in patients with proliferative diabetic retinopathy (PDR) [38]. In rat retinal tissue, the succinate content in ischemic retinas was 3.3 times higher than those in controls (19.6 ± 2.2 μM vs. 5.6 ± 0.3 μM) [39].Upon cell necrosis or transport-mediated export, neighboring macrophages are exposed to millimolar levels [40]. Consequently, most in vitro studies utilize 0.2–10 mM succinate for intervention [41–43]. In our previous work, we conducted concentration gradient experiments (0.5–2 mM) and identified that 1 mM succinate for 48 h induced the most significant pro-fibrotic M2 polarization [8]. Regarding lactate, although levels in mouse RPE-choroid rise from 0.6 mM to 0.9 mM in CNV lesions [12], concentrations in hypoxic tumor microenvironments or bacterial environments can reach 10–40 mM [44,45]. In vitro studies on macrophage polarization commonly employ lactate concentrations ranging from 10

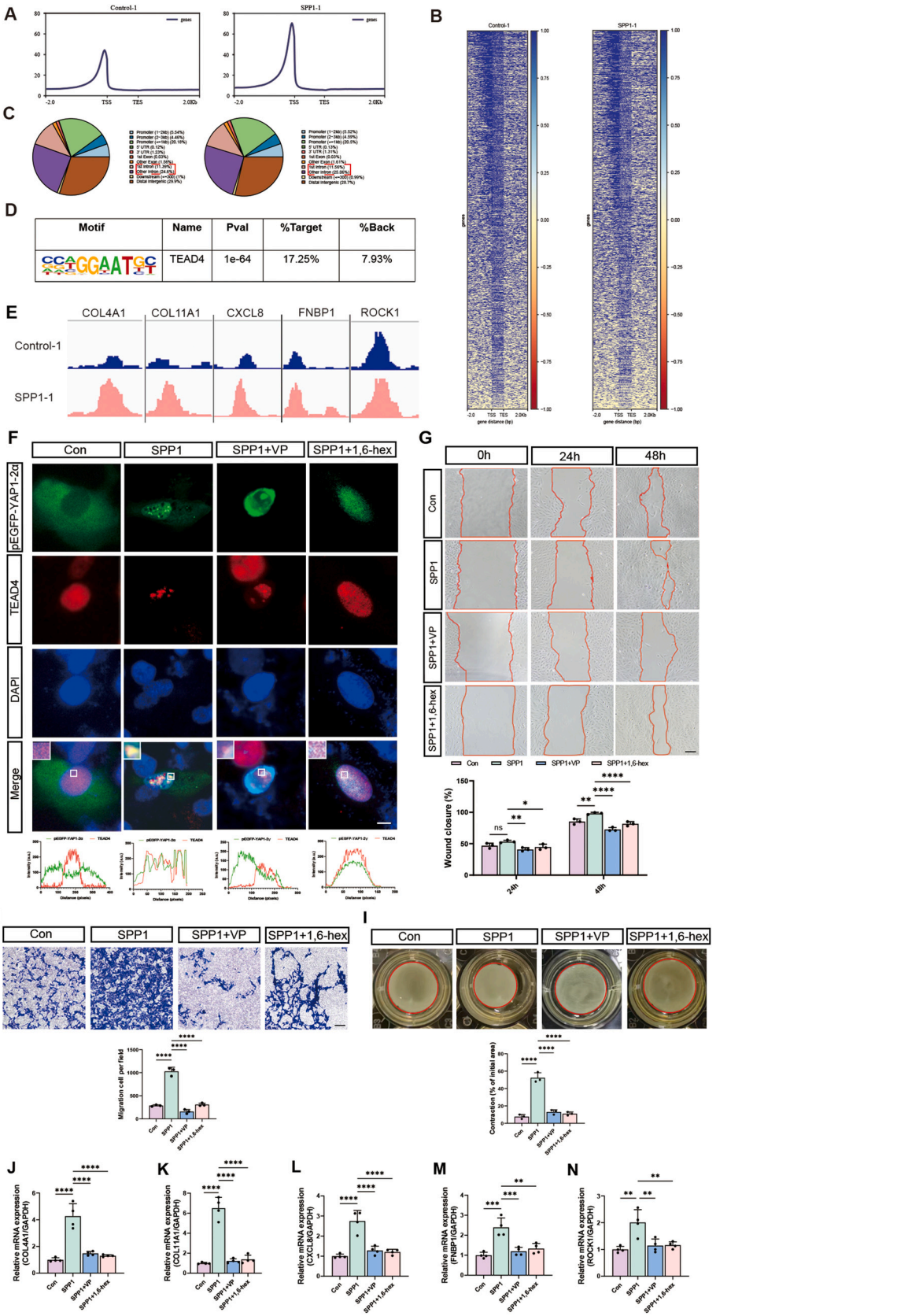

(caption on next page)

Fig. 7. YAP1-TEAD4 interaction promotes SPP1-induced RPE-EMT. (A) Average enrichment profiles of mapped reads surrounding transcription start sites (TSS). (B) Heatmap illustrating the density of mapped reads across gene loci. (C) Genomic distribution of ATAC-seq peaks across various functional categories. (D) Transcription factor (TF) motif enrichment analysis of peaks significantly upregulated in SPP1-treated cells versus control. (E) Representative ATAC-seq tracks displaying accessibility at the intronic regions of target genes in control and SPP-treated RPE cells (48 h). Scale for visualization: FNBP1 (0–140), COL11A1 (0–70), COL4A1 (0–220), ROCK1 (0–180), and CXCL8 (0–120). (F) Representative immunofluorescence images demonstrating the colocalization of YAP1–2α (green) and TEAD4 (red) in RPE cells following SPP1 treatment with or without 10 μM verteporfin or 5% 1,6-hexanediol. Nuclei were counterstained with DAPI (blue). Scale bar: 10 μm.(G) Representative images of wound healing assays in different ARPE-19 treatment groups at 24 and 48 h post-treatment (n = 3). Scale bar: 50 μm. (H) Representative images of Transwell migration assays in different ARPE-19 treatment groups at 48 h post-treatment (n = 3). Scale bar: 50 μm. (I) Representative images comparing collagen gel contraction in different ARPE-19 treatment groups at 48 h post-release from culture plates (n = 3). (J–N) qPCR analysis of the expression of representative pro-fibrotic genes (COL4A1, COL11A1, CXCL8, FNBP1, and ROCK1) identified as transcriptional targets through ATAC-seq analysis. The data were analyzed via one-way ANOVA with Bonferroni analysis. $^{*}P < 0.05$, $^{**}P < 0.01$, $^{***}P < 0.001$, $^{****}P < 0.0001$. (For interpretation of the references to color in this figure legend, the reader is referred to the web version of this article.)

to 25 mM [46,47]. In our study, we observed that 20 mM lactate for 6 h elicited the most pronounced pro-fibrotic M2 polarization.

Current research suggested that the transcriptional co-activator YAP1 played a pivotal role in maintaining progenitor cell proliferation and dedifferentiation. In RPE cells, YAP1 was proved to be essential for maintaining adult RPE differentiation. It was critical for preserving apical polarity, tight junctions, and the expression of the RPE cell marker RPE65 [48–50]. However, existing studies on YAP1 function in RPE cells have largely focused on its regulation of RPE cell differentiation fate and the activation of the RhoA/YAP1 pathway in promoting RPE-EMT [51,52]. Consequently, we broadened our scope to examine the behavior of YAP1 during SPP1 treatment, observing significant nuclear translocation. Previous studies revealed that YAP1 possesses nine distinct isoforms, which exhibit variations in subcellular localization, cellular function, and capacity to undergo LLPS [22]. Specifically, only YAP1–1α and YAP1–2α containing functional leucine zippers within their coiled-coil domains render them prone to LLPS [53]. A study on cancer stemness reported a shift in mRNA dominance from YAP1–2γ to YAP1–2α under genotoxic stress. This shift was driven by the formation of specific super-enhancers binding to the TEAD family, which enhanced cancer stem-like properties. [53]. Based on this, we investigated whether a similar isoform switch occurred in RPE cells. We found that under SPP1 stimulation, there is a shift in mRNA dominance from YAP1–1α to YAP1–2α. Our findings clarify that YAP1–2α is the dominant isoform driving the RPE-EMT process in the context of SPP1 intervention. Importantly, while YAP1 itself lacks DNA-binding domains, it activates downstream transcription through interactions with sequence-specific transcription factors, most notably members of the TEAD family [54,55]. In our study, ATAC-seq analysis revealed a high enrichment of TEAD4 binding motifs within the differentially accessible chromatin regions following SPP1 treatment. Previous research has revealed that the YAP1–2α/TAZ/TEAD4 complex forms the core of super-enhancers that initiate reversible EMT in tumor cells [23]. This complex activates key EMT-inducing transcription factors [56–58], driving cells toward a hybrid or partial EMT state. Consistently, we found that SPP1 treatment induced the nuclear translocation of YAP1 in RPE cells and its significant colocalization with TEAD4, resulting in the RPE-EMT characteristics. Crucially, both the blockade of LLPS and the inhibition of YAP-TEAD4 binding reversed these phenotypic changes, confirming the pivotal role of the YAP1-TEAD4 complex in RPE-EMT progression.

To elucidate the mechanism underlying SPP1-induced YAP1–2α/TEAD4 super-enhancer formation, we used bioinformatics analysis and identified CD44 as the receptor mediating SPP1-RPE interactions, revealing that YAP1 upregulation occurred through CD44/RhoA pathway activation. Previous studies have reported CD44 acted as both an upstream regulator and a downstream effector of YAP1, and this feedback loop regulates cell proliferation and invasion during carcinogenesis [59,60]. These findings establish a positive correlation between CD44 and YAP1 expression, suggesting potential regulatory crosstalk. Experimental evidence has demonstrated that CD44 altered the subcellular distribution of YAP1 through RhoA-mediated mechanisms [61]. These suggest that targeting the CD44/RhoA/YAP1 axis offers a promising therapeutic strategy to prevent SRF.

At present, there are no specific treatments for SRF. Current clinical management remains predominantly focused on anti-VEGF therapy for CNV, while the primary reason for non-response to anti-VEGF therapy is the occurrence of SRF. Our preclinical study provides new information for novel clinical interventions. Firstly, our data suggested that SPP1 could serve as a biomarker for predicting the trajectory of SRF. Secondly, we have identified the CD44/RhoA/YAP1 axis as a novel therapeutic target. Thirdly, we found that YAP1 LLPS could be disrupted by VP to attenuate EMT-related phenotypes. Currently, VP is used in photodynamic therapy to treat CNV in nAMD. Our study revealed another potential mechanism of action for VP, specifically for inhibiting the development of SRF.

4.1. Limitations

There is an inherent disparity between the complex, multicellular physiological immune microenvironment in vivo and in vitro intervention model in our study. We simulated in vitro using only a single acidic metabolite, which is far from covering the multicellular and highly complex immune microenvironment in vivo. Therefore, the co-culture system of $SPP1^{+}$ macrophages and RPE cells in vitro, and SPP1 macrophage conditional knockout mice in vivo, are still needed for further validation. Another limitation in our mechanistic investigation concerns the pharmacological tools targeting the YAP1–2α isoform. Current inhibitors, such as verteporfin and 1,6-hexanediol, lack high selectivity for YAP1–2α relative to other functional YAP1 isoforms. Consequently, while we observed that disrupting YAP1-TEAD4 interaction or inhibiting LLPS attenuates RPE-EMT, we cannot entirely exclude the roles of other YAP1 isoforms in this process.

4.2. Future directions

Based on our current findings, there are still some research directions that can be further improved. Firstly, future studies could validate the diagnostic and prognostic potential of SPP1 as a clinical biomarker using human vitreous and subretinal fluid samples from nAMD and SRF patients. Secondly, our ATAC-seq analysis revealed that chromatin accessibility at the promoter regions of chromatin remodeling-related genes was significantly increased in the SPP1 intervention group. This suggests that these target genes may, in turn, further influence chromatin accessibility, forming a positive feedback loop that warrants further investigation. Ultimately, future investigations should employ isoform-specific knockdown via specialized siRNA or CRISPR-Cas9 sequences, or develop more selective small-molecule inhibitors that specifically target the YAP1–2α isoform without cross-reacting with other variants.

5. Conclusion

In conclusion, our study identifies a novel macrophage-RPE crosstalk mechanism that drives the progression of SRF. We demonstrate that acidic metabolites, succinate and lactate, prompt macrophages to secrete SPP1, which activates the CD44/RhoA signaling axis in RPE cells. This activation leads to the upregulation and nuclear translocation

of the YAP1–2α isoform, which forms condensates that bind to TEAD4. In turn, this complex targets open chromatin regions, specifically intronic enhancers, to promote the transcription of pro-fibrotic genes. Notably, we provide evidence that these events occur under the acidic metabolic conditions of the pathological microenvironment by elucidating the SPP1/CD44 axis as a central driver of RPE-EMT. Furthermore, we are the first to identify YAP1–2α as the predominant isoform within RPE cells in this microenvironment. Our findings offer molecular insights into the pathogenesis of fibrotic ocular diseases and suggest potential therapeutic targets for nAMD patients resistant to anti-VEGF therapies.

CRediT authorship contribution statement

Ruoyi Lin: Writing – review & editing, Writing – original draft, Visualization, Validation, Data curation, Conceptualization. **Zixin Cai:** Writing – review & editing, Writing – original draft, Formal analysis, Data curation, Conceptualization. **Tianyu Zheng:** Writing – original draft, Visualization, Validation, Data curation, Conceptualization. **Yan Wu:** Writing – review & editing, Writing – original draft, Formal analysis, Data curation, Conceptualization. **Zihang Xu:** Writing – review & editing, Writing – original draft, Formal analysis, Data curation, Conceptualization. **Yunhong Luo:** Writing – review & editing, Writing – original draft, Formal analysis, Data curation, Conceptualization. **Feng Liang:** Writing – original draft, Methodology, Formal analysis, Data curation. **Manhui Zhu:** Writing – review & editing, Writing – original draft, Formal analysis, Data curation, Conceptualization. **Jing Yu:** Writing – review & editing, Funding acquisition. **Wenting Cai:** Writing – review & editing, Funding acquisition, Data curation, Conceptualization.

Declaration of competing interest

None.

Acknowledgments

This work was supported by research from the Clinical Research Project of the Shanghai Municipal Health Commission (grant number 20244Y0223), the Bethune Langmu Young Ophthalmology Research Fund of China (grant number BCF-KH-YK-20240906-08), the Pudong New Area Science and Technology Development Fund (PKJ2025-Y47), the Pudong New Area Science and Education-driven Medical Development Cultivation Project (PWXx2025-01), and Integrated Traditional Chinese and Western Medicine Guidance Project in General Hospitals (ZHYYZXYYD-202513).

Appendix A. Supplementary data

Supplementary data to this article can be found online at https://doi.org/10.1016/j.metabol.2026.156648.

Data availability

Data supporting the present study are available from the corresponding author upon reasonable request.

References

[1] Apte RS. Reducing treatment burden in AMD. Cell 2020;180(6):1033.
[2] Cheong KX, Cheung CMG, Teo KYC. Review of fibrosis in neovascular age-related macular degeneration. Am J Ophthalmol 2023;246:192–222.
[3] Kent D, Sheridan C. Choroidal neovascularization: a wound healing perspective. Mol Vis 2003;9:747–55.
[4] Shu DY, Butcher E, Saint-Geniez M. EMT and EndMT: emerging roles in age-related macular degeneration. Int J Mol Sci 2020;21(12).
[5] Cherepanoff S, et al. Bruch's membrane and choroidal macrophages in early and advanced age-related macular degeneration. Br J Ophthalmol 2010;94(7):918–25.
[6] Li H, Li B, Zheng Y. Role of microglia/macrophage polarisation in intraocular diseases (review). Int J Mol Med 2024;53(5).
[7] Cao X, et al. Macrophage polarization in the maculae of age-related macular degeneration: a pilot study. Pathol Int 2011;61(9):528–35.
[8] Shen T, et al. Succinate-induced macrophage polarization and RBP4 secretion promote vascular sprouting in ocular neovascularization. J Neuroinflammation 2023;20(1):308.
[9] Li X, et al. Correction: lactate metabolism in human health and disease. Signal Transduct Target Ther 2022;7(1):372.
[10] Heuser C, et al. Targeting lactate metabolism for cancer immunotherapy - a matter of precision. Semin Cancer Biol 2023;88:32–45.
[11] Leveillard T, Philp NJ, Sennlaub F. Is retinal metabolic dysfunction at the center of the pathogenesis of age-related macular degeneration? Int J Mol Sci 2019;20(3).
[12] Song J, et al. Lactic acid upregulates VEGF expression in macrophages and facilitates choroidal neovascularization. Invest Ophthalmol Vis Sci 2018;59(8):3747–54.
[13] Mia MM, Singh MK. New insights into hippo/YAP signaling in fibrotic diseases. Cells 2022;11(13).
[14] Cai D, et al. Phase separation of YAP reorganizes genome topology for long-term YAP target gene expression. Nat Cell Biol 2019;21(12):1578–89.
[15] Mao S, et al. Phase separation of YAP mediated by coiled-coil domain promotes hepatoblastoma proliferation via activation of transcription. J Gastroenterol Hepatol 2023;38(8):1398–407.
[16] Zhuge R, et al. hCINAP regulates the differentiation of embryonic stem cells by regulating NEDD4 liquid-liquid phase-separation-mediated YAP1 activation. Cell Rep 2023;42(1):111935.
[17] Chen W, et al. The cancer-associated fibroblast facilitates YAP liquid-liquid phase separation to promote cancer cell stemness in HCC. Cell Commun Signal 2025;23(1):238.
[18] Little K, et al. A two-stage laser-induced mouse model of subretinal fibrosis secondary to choroidal neovascularization. Transl Vis Sci Technol 2020;9(4):3.
[19] Zhang X, Goncalves R, Mosser DM. The isolation and characterization of murine macrophages. Curr Protoc Immunol 2008;83:14.1.1–14.1.14.
[20] Li Y, et al. Severe lung fibrosis requires an invasive fibroblast phenotype regulated by hyaluronan and CD44. J Exp Med 2011;208(7):1459–71.
[21] Li S, et al. Targeting mechanics-induced fibroblast activation through CD44-RhoA-YAP pathway ameliorates crystalline silica-induced silicosis. Theranostics 2019;9(17):4993–5008.
[22] Vrbsky J, et al. Evidence for discrete modes of YAP1 signaling via mRNA splice isoforms in development and diseases. Genomics 2021;113(3):1349–65.
[23] Thrash HL, Pendergast AM. Multi-functional regulation by YAP/TAZ signaling networks in tumor progression and metastasis. Cancers (Basel) 2023;15(19).
[24] Ramachandran P, et al. Resolving the fibrotic niche of human liver cirrhosis at single-cell level. Nature 2019;575(7783):512–8.
[25] Morse C, et al. Proliferating SPP1/MERTK-expressing macrophages in idiopathic pulmonary fibrosis. Eur Respir J 2019;54(2).
[26] Huang HY, et al. Alternations in inflammatory macrophage niche drive phenotypic and functional plasticity of Kupffer cells. Nat Commun 2024;15(1):9337.
[27] Palma A. The landscape of SPP1 (+) macrophages across tissues and diseases: a comprehensive review. Immunology 2025;176(2):179–96.
[28] Luo S, et al. Piezo1 specific deletion in macrophage protects the progression of liver fibrosis in mice. Theranostics 2023;13(15):5418–34.
[29] He Y, et al. Myeloid Piezo1 deletion protects renal fibrosis by restraining macrophage infiltration and activation. Hypertension 2022;79(5):918–31.
[30] Zhang Y, et al. Piezo1-mediated mechanotransduction promotes cardiac hypertrophy by impairing calcium homeostasis to activate calpain/calcineurin signaling. Hypertension 2021;78(3):647–60.
[31] Murthy S, et al. Danger signal extracellular calcium initiates differentiation of monocytes into SPP1/osteopontin-producing macrophages. Cell Death Dis 2022;13(1):53.
[32] Ma C, et al. Gastrodin alleviates NTG-induced migraine-like pain via inhibiting succinate/HIF-1alpha/TRPM2 signaling pathway in trigeminal ganglion. Phytomedicine 2024;125:155266.
[33] Byun KA, et al. Piezo1 activation drives enhanced collagen synthesis in aged animal skin induced by poly L-lactic acid fillers. Int J Mol Sci 2024;25(13).
[34] Petsophonsakul P, et al. Nicotine promotes vascular calcification via intracellular Ca2+-mediated, Nox5-induced oxidative stress, and extracellular vesicle release in vascular smooth muscle cells. Cardiovasc Res 2022;118(9):2196–210.
[35] Deng G, et al. BET inhibitor suppresses melanoma progression via the noncanonical NF-kappaB/SPP1 pathway. Theranostics 2020;10(25):11428–43.
[36] Safran JB, Butler WT, Farach-Carson MC. Modulation of osteopontin post-translational state by 1, 25-(OH)2-vitamin D3. Dependence on Ca2+ influx. J Biol Chem 1998;273(45):29935–41.
[37] Riemann A, et al. The role of microRNAs in gene expression and signaling response of tumor cells to an acidic environment. Int J Mol Sci 2023;24(23).
[38] Matsumoto M, et al. Succinate increases in the vitreous fluid of patients with active proliferative diabetic retinopathy. Am J Ophthalmol 2012;153(5):896–902 e1.
[39] Sapieha P, et al. The succinate receptor GPR91 in neurons has a major role in retinal angiogenesis. Nat Med 2008;14(10):1067–76.
[40] Tretter L, Patocs A, Chinopoulos C. Succinate, an intermediate in metabolism, signal transduction, ROS, hypoxia, and tumorigenesis. Biochim Biophys Acta 2016;1857(8):1086–101.
[41] Mills EL, et al. Succinate dehydrogenase supports metabolic repurposing of mitochondria to drive inflammatory macrophages. Cell 2016;167(2):457–470 e13.
[42] Keiran N, et al. SUCNR1 controls an anti-inflammatory program in macrophages to regulate the metabolic response to obesity. Nat Immunol 2019;20(5):581–92.

[43] Yang W, et al. Succinic acid-induced macrophage endocytosis promotes extracellular vesicle-based integrin beta1 transfer accelerating fibroblast activation and sepsis-associated pulmonary fibrosis. Adv Sci (Weinh) 2025;12(43):e07411.
[44] Okada T, et al. Microbiota-derived lactate accelerates colon epithelial cell turnover in starvation-refed mice. Nat Commun 2013;4:1654.
[45] Brizel DM, et al. Elevated tumor lactate concentrations predict for an increased risk of metastases in head-and-neck cancer. Int J Radiat Oncol Biol Phys 2001;51(2):349–53.
[46] Shi W, et al. Lactic acid induces transcriptional repression of macrophage inflammatory response via histone acetylation. Cell Rep 2024;43(2):113746.
[47] Zhang D, et al. Metabolic regulation of gene expression by histone lactylation. Nature 2019;574(7779):575–80.
[48] Lu Q, et al. Yap1 is required for maintenance of adult RPE differentiation. FASEB J 2020;34(5):6757–68.
[49] Kim JY, et al. Yap is essential for retinal progenitor cell cycle progression and RPE cell fate acquisition in the developing mouse eye. Dev Biol 2016;419(2):336–47.
[50] Miesfeld JB, et al. Yap and Taz regulate retinal pigment epithelial cell fate. Development 2015;142(17):3021–32.
[51] Gelat Brijesh, Malaviya Pooja, Rathaur Pooja, Trivedi Krupali, Chaudhary Priya, Patel Binita, et al. Regulation of epithelial-mesenchymal transition in retinal pigment epithelium and its associated cellular signaling cascades: an updated review. Beni-Suef Univ J Basic Appl Sci 2023;12.
[52] Yang N, et al. Construction and analysis of mRNA, lncRNA, and transcription factor regulatory networks after retinal ganglion cell injury. Exp Eye Res 2022;215:108915.
[53] Ben C, et al. Alternative splicing reverses the cell-intrinsic and cell-extrinsic pro-oncogenic potentials of YAP1. J Biol Chem 2020;295(41):13965–80.
[54] Barrette AM, et al. Anti-invasive efficacy and survival benefit of the YAP-TEAD inhibitor verteporfin in preclinical glioblastoma models. Neuro Oncol 2022;24(5):694–707.
[55] Zhao B, et al. TEAD mediates YAP-dependent gene induction and growth control. Genes Dev 2008;22(14):1962–71.
[56] Lau AN, et al. Tumor-propagating cells and Yap/Taz activity contribute to lung tumor progression and metastasis. EMBO J 2014;33(5):468–81.
[57] Shao DD, et al. KRAS and YAP1 converge to regulate EMT and tumor survival. Cell 2014;158(1):171–84.
[58] Matteucci E, et al. Bone metastatic process of breast cancer involves methylation state affecting E-cadherin expression through TAZ and WWOX nuclear effectors. Eur J Cancer 2013;49(1):231–44.
[59] Lai CJ, et al. CD44 promotes migration and invasion of docetaxel-resistant prostate cancer cells likely via induction of hippo-yap signaling. Cells 2019;8(4).
[60] Fan Z, et al. Standard CD44 modulates YAP1 through a positive feedback loop in hepatocellular carcinoma. Biomed Pharmacother 2018;103:147–56.
[61] Zhang Y, et al. CD44 acts through RhoA to regulate YAP signaling. Cell Signal 2014;26(11):2504–13.